Online Resource 1 Supplementary information

Spectral overlap and molecular sampling in Raman enhancement at nanoparticle oxide metal interfaces

Patrícia M. A. Farias; Priscila Vilemen; Nathalia B. Lima; Andreas Stingl; Olavo Cardozo

Plasmonics

Corresponding author: Patrícia M. A. Farias, Laboratory for Advanced Materials, Graduate Program on Materials Science, Federal University of Pernambuco (UFPE), Recife, PE 50670-901, Brazil. E-mail: patricia.mafarias@ufpe.br

S1 Scope and provenance

This supplement provides independent analytical verification and full-wave benchmarks for the prescribed geometry. The benchmarks were generated from the stated dimensions and material datasets. The executable code, exact material tables, numerical inputs, complex electric fields, outgoing multipole coefficients, convergence runs and derived data are supplied in Online Resource 2. A numerical convergence check verifies stability under the tested discretizations; it is not experimental validation or an independent second-solver comparison.

S2 Spectral model and exact optimization

Let s denote optical wavenumber in cm^{-1}, $\tilde{\nu}$ the Stokes shift, H a prescribed local-intensity peak height and h its half-width at half-maximum. The excitation and reciprocal intensity transfer functions are identical Lorentzians in this reduced model. They are not extinction spectra.

$$G(s) = H/[1 + ((s - s_c)/h)^2] \; ; \qquad K = G(s^L)G(s^L - \tilde{\nu}) \quad \text{(S1)}$$

Set $a = \tilde{\nu}/(2h)$, $s_m = s^L - \tilde{\nu}/2$ and $u = (s_c - s_m)/h$. Then $K = H^2/D(u)$, where

$$D(u) = u^4 + 2(1 - a^2)u^2 + (1 + a^2)^2 \; ; \qquad D'(u) = 4u(u^2 + 1 - a^2) \quad \text{(S2)}$$

For $a \le 1$ the minimum denominator occurs at $u = 0$. For $a > 1$ it occurs at $u = \pm\sqrt{(a^2 - 1)}$. At $a = 1$ the stationary midpoint remains optimal with a vanishing quadratic curvature. Substitution gives

$$K_{max}/H^2 = (1 + a^2)^{-2} \; for \; a \le 1 \; ; \qquad K_{max}/H^2 = 1/(4a^2) \; for \; a > 1 \quad \text{(S3)}$$

For $\tilde{\nu} = 1580\ cm^{-1}$, candidate A uses H = 100 and h = 200 cm^{-1}; candidate B uses H = 60 and h = 800 cm^{-1}. A is initially pump-centred and B midpoint-centred. Independent bounded numerical optimization agrees with the closed-form maxima to a relative difference below 10^{-12}. A separate dense-grid check was supplied with the revised manuscript.

Table S1. Independently verified spectral results. The apparent nonzero midpoint offset from a bounded numerical optimizer is below 0.0001 cm^{-1} and is numerical rounding.

Quantity	A	B
a	3.95	0.9875
Initial K	157.703832	922.783002
Optimized K	160.230732	922.783002
Optimal $\lvert s_c - s_m \rvert$ (cm^{-1})	764.26435	0

The initial ratio is 5.851367016; after independent optimization it is 5.759088716. The occupancy/projection threshold is 0.173638582. These quantities concern prescribed local transfer functions. A measured extinction curve alone does not supply H or h for such a local function.

$$\lambda_s = 10^7/(10^7/\lambda^L - \tilde{\nu}) \quad \text{(S4)}$$

Table S2. Vacuum wavelengths for ν̃= 1580 cm⁻¹. Wavenumbers are reciprocal vacuum wavelengths.

Pump (nm)	Stokes (nm)
532	580.821534941
633	703.344274244
785	896.149411510

S3 Molecular kernel and spatial statistics

The normalized amplitude for detected mode j is the reciprocal bilinear contraction f_rec,j · α̂R · f_exc. For the prescribed x-directed rank-one Raman tensor and x-polarized detection, K = |Ex(ωL)|² |Ex(ωS)|². The site distribution is held fixed between the two frequencies. For two sites with weights w and 1 − w,

$$\bar{K} = wG_1^L G_{S,1} + (1-w)G_2^L G_{S,2} \quad \text{(S5)}$$

$$K_{sep} = [wG_1^L + (1-w)G_2^L][wG_{S,1} + (1-w)G_{S,2}] \quad \text{(S6)}$$

$$\bar{K} - K_{sep} = w(1-w)(G_1^L - G_2^L)(G_{S,1} - G_{S,2}) \quad \text{(S7)}$$

The relative underestimate is 100(1 − Ksep/K̄)%. Its denominator is the correct registered mean product. The identity was independently tested for 1000 random positive two-site arrays and weights. In the manuscript example, GL = (1000,10), and GS is either (400,40) or (40,400). At equal weights, K̄ is 200200 or 22000, whereas Ksep remains 111100. Their ratio is exactly 9.10.

S4 Full-wave geometry materials and normalization

SMUTHI (Scattering by Multiple Particles in Thin-Film Systems) 2.2.4, is a Python package that solves the frequency-domain Maxwell multiple-scattering problem by combining analytical spherical T matrices with planar-layer scattering matrices [S1]. No point-dipole, quasistatic-image or stationary-phase approximation is used in the reported benchmark. The finite spheres are not periodically repeated.

Table S3. Prescribed model inputs. The geometry is an idealized benchmark, not a measured reconstruction.

Input	Specified value
Sphere radius	60 nm (diameter 120 nm)
Sphere centres	(−70,0,68) and (70,0,68) nm
Surface gap between spheres	20 nm
Aluminium	Half-space z < 0
Oxide	0 < z < 3 nm; constant n = 1.65; no absorption
Ambient and optical spacer	Air n = 1; 5 nm between sphere bottom and oxide
Reporter 1 inward	(−9,0,68) nm
Reporter 2 outward	(−131,0,68) nm
Excitation	−z propagation; x polarization; unit incoming E
Detection and reciprocity	Outgoing +z x-polarized mode; reciprocal incidence −z
Raman tensor	Normalized x ⁻ ¹x; shift 1580 cm

The gold n and k values are linearly interpolated in vacuum wavelength from the Johnson–Christy table [S2]. Aluminium is interpolated from the tabulated Rakić Lorentz–Drude dataset [S3]. Both exact tables are included, with SHA-256 hashes in the environment records. The prescribed nonabsorbing oxide is an idealization, not a measurement of the actual foil. Air controls retain the coordinates and molecular reference of the supported controls.

All electric fields use the time convention $\exp(-i\omega t)$ and incoming amplitude unity at the origin. Pump and reciprocal Stokes solutions are separate frequency-domain solves. For this air-incident x-directed single-mode reference the homogeneous molecular kernel is unity. No bare-foil intensity renormalization is introduced. Such a renormalization would change the reported interaction diagnostic and must not be mixed with these values.

S5 Numerical controls and convergence

For numerical stability, we also solve the same assembled system after the diagonal similarity transformation $b = S\,y$, where S is the square root of the absolute diagonal spherical T-matrix. The transformed system is $S^{-1}MS\,y = S^{-1}rhs$. This changes the numerical scale of the unknowns, not the physical coupling model. Unscaled high-order LU runs showed unstable air-pair fields despite small residuals and are retained only as diagnostics; the selected results use the rescaled solution. The direct LU solution retains the dense coupling matrix and the full azimuthal multipole range mmax = lmax. The archive includes multipole-cutoff scans and a separate Sommerfeld-contour truncation test and a joint refinement of contour step and field angular quadrature. Solving the linear algebra accurately is necessary but does not establish truncation convergence. Reported residuals are $\|Mb - rhs\|_2/\|rhs\|_2$ for the assembled system $M = I - TW$.

The selected run uses lmax = mmax = 18, effective-index truncation 40, maximum contour step 0.02, imaginary contour depth 0.1, and 96 azimuthal intervals for reflected-field evaluation. Exact contour construction is provided by the retained solver source and environment records. Matrix assembly and coefficients use double precision; reflected-field evaluation uses the solver CPU default single precision, with its retained accuracy tested by field quadrature changes and an independent Fresnel calculation. Displayed extra digits facilitate reproduction and do not represent uncertainty in material inputs.

The final smooth-contour multipole refinement and independent contour-deformation/quadrature comparison each change all registered projected intensities and kernels by less than 0.5% over the four controls, two sites and both frequency pairs. This is numerical self-convergence under the tested refinements, not proof of exactness or experimental validation.

Table S4. Changes under numerical refinement, maximized over all four controls, both sites and both frequency pairs. Gx comparisons include all four wavelengths.

Comparison	Max relative Gx change (%)	Max relative K change (%)
Contour truncation 20 to 40 at L12	0.026315	0.043977
Unscaled versus rescaled LU at L12	0.0034544	0.002588
Rescaled multipoles 12 to 16	0.2626	0.51472
Coarse-contour L16 versus fine-contour L18	0.93857	0.5101
Smooth-contour multipoles 16 to 18	0.046329	0.063945
Independent contour deformation and quadrature	0.086437	0.15139

An independent normal-incidence Fresnel calculation agrees with the bare-layer background to a maximum relative difference of 9.34×10^{-8}. The selected assembled-system residual is at most 1.36×10^{-15}. Stored complex fields reproduce their JSON intensities exactly within the recorded reconstruction check.

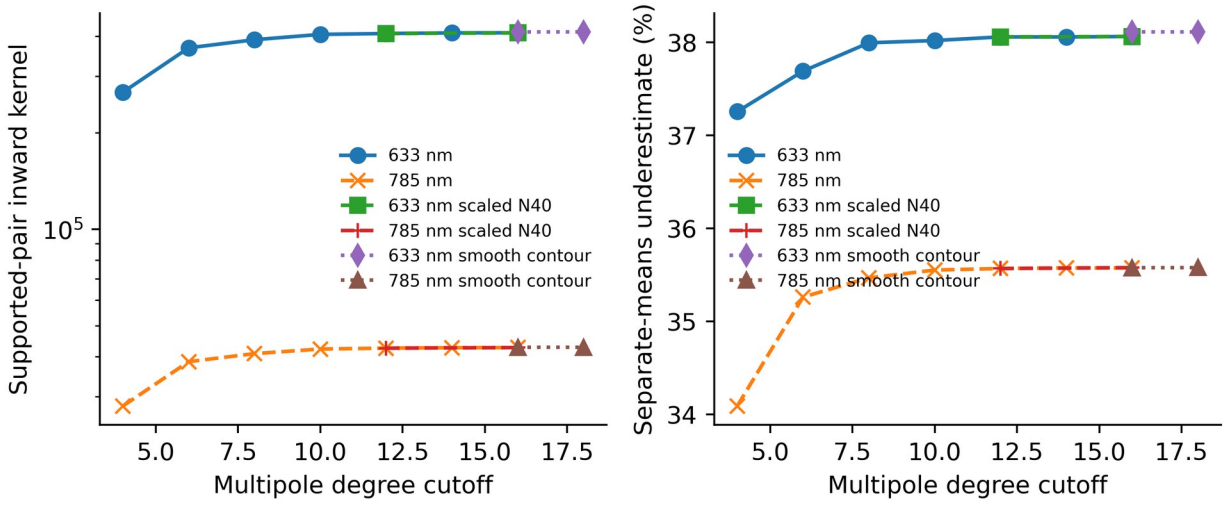


Fig. S1 Multipole-cutoff scan for the baseline truncation 20, contour step 0.02 and 96 azimuthal intervals, together with rescaled runs at truncation 40. Baseline unscaled high-order ratios are not selected. These curves alone do not establish contour-tail convergence. Additional independent refinements are tabulated in Table S4

S6 Registered pump and Stokes fields and response kernels

Table S5 is computed directly from the complex fields retained in the selected NPZ files. The CSV complex_fields.csv includes every total-field Cartesian component and its run identifier. The linked NPZ files additionally contain background and scattered fields and the multipole coefficients. The two sites remain fixed between pump and Stokes calculations. Equal weighting is used only when forming the two-site means.

Table S5a. Full-wave intensities and kernels at 633 nm pump and 703.344274 nm Stokes. Selected numerical run: contour_L18_N40_d0.02_P96.

Control	Site	GL	GS	K
Air monomer	Inward	22.3571	17.5114	391.504
Air monomer	Outward	22.3571	17.5114	391.504
Air pair	Inward	225.552	163.097	36786.9
Air pair	Outward	29.448	26.714	786.675
Supported monomer	Inward	70.2464	38.2818	2689.16
Supported monomer	Outward	70.2464	38.2818	2689.16
Supported pair	Inward	572.091	720.628	412265
Supported pair	Outward	84.1333	67.7621	5701.05

Table S5b. Full-wave intensities and kernels at 785 nm pump and 896.149412 nm Stokes. Selected numerical run: contour_L18_N40_d0.02_P96.

Control	Site	GL	GS	K
Air monomer	Inward	14.6781	12.6439	185.588
Air monomer	Outward	14.6781	12.6439	185.588
Air pair	Inward	117.338	86.3161	10128.2
Air pair	Outward	22.2164	18.3087	406.754
Supported monomer	Inward	23.9824	16.7968	402.829
Supported monomer	Outward	23.9824	16.7968	402.829
Supported pair	Inward	292.08	146.475	42782.3
Supported pair	Outward	38.4838	23.8602	918.229

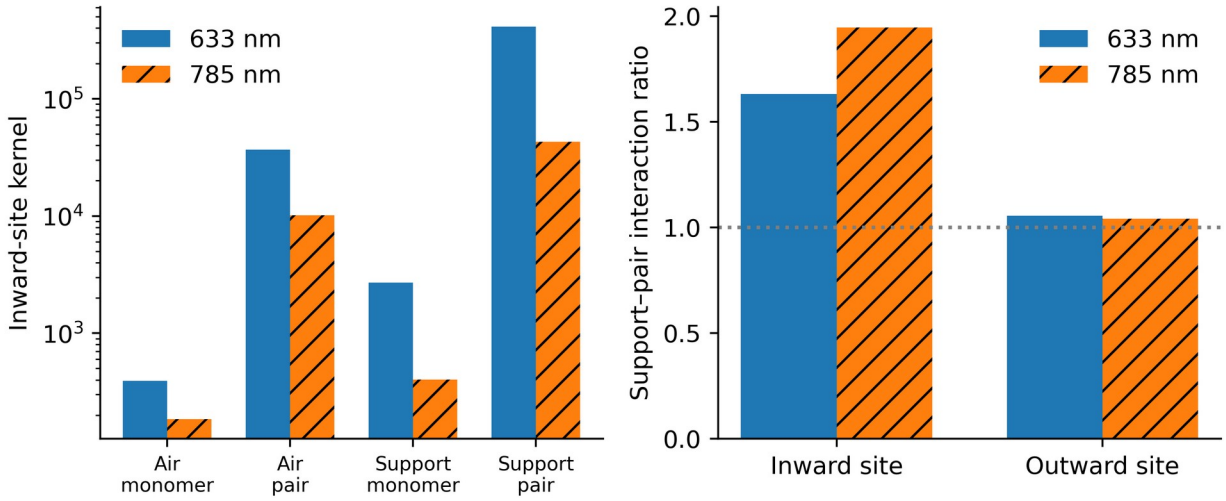


Fig. S2 Full-wave inward-site kernels for all four controls and interaction ratios at the two reporter sites. The dotted unity line denotes multiplicative separability. The plot uses the selected refinement run identified in Tables S5a and S5b

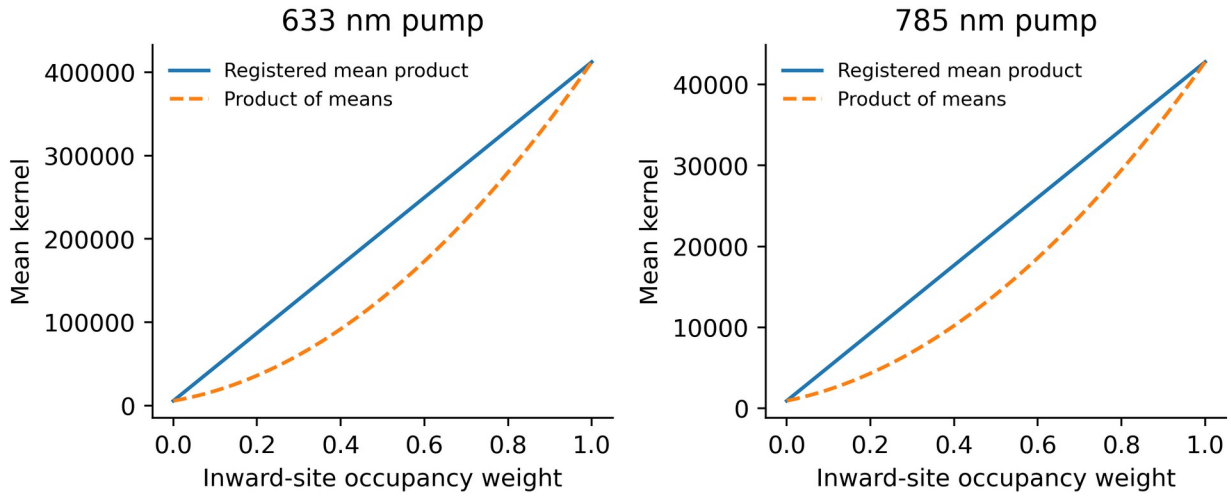


Fig. S3 Dependence of the supported-pair mean kernel on the inward-site occupancy weight. Solid curves retain spatial registration; dashed curves multiply separately averaged fields. The w = 0.5 comparison corresponds to the two-site means in main-text Table 4.

S7 Wavelength scan and geometry sensitivity design

The extended calculations retain the radius, material tables, normal-incidence x polarization, x-directed rank-one Raman tensor, single back-collected mode and two reporter sites of the main model. The baseline is (t,s,g) = (3,5,20) nm. The baseline and the two endpoints of each parameter range are scanned from 500 to 900 nm in 25 nm steps, including 633 and 785 nm explicitly. Additional 5 nm sampling surrounds the sampled mean-kernel maxima; the baseline pump-only and upward-scattering maxima are also refined. The two interior levels of each parameter are evaluated at 633 and 785 nm. This is a one-factor-at-a-time design, not a factorial response surface.

Table S6. Extended geometry design. All parameters other than the varied factor retain their nominal values.

Parameter	Five levels (nm)	Nominal (nm)	Finite-difference step (nm)
Oxide t	1, 2, 3, 4, 5	3	1
Air spacer s	3, 4, 5, 6, 7	5	1
Interparticle gap g	10, 15, 20, 25, 30	20	5

The sphere centres are $(\pm(60 + g/2), 0, 60 + t + s)$ nm. The inward and outward reporter coordinates relative to the left-particle centre are (+61,0,0) and (−61,0,0) nm. Thus every sweep retains a reporter 1 nm outside gold; oxide and spacer variation do not inadvertently change that molecular distance. The optical spacer remains air with refractive index 1, while the oxide retains a real, wavelength-independent refractive index of 1.65. These are prescribed optical inputs, not measured residue or oxide compositions.

At each pump wavelength, a separate calculation is performed at $\lambda_s = 10^7/(10^7/\lambda^L - 1580)$ nm. The primary objective is $\bar{K} = \tfrac{1}{2}\Sigma_i G^L{}_{,i} G_{s,i}$. The single-frequency proxy is $\tfrac{1}{2}\Sigma_i G^L{}_{,i}{}^2$, rather than the square of a separately averaged field. The local sensitivities in main-text Eq. (17) use the central steps in Table S6. Peak wavelengths refer to the sampled grid, not a fitted analytical resonance or a proven global optimum.

The upward particle-scattering cross-section is computed from the outgoing multipole coefficients and the planar-layer response, integrated over air-side polar angles from 10^{-5} to $\pi/2 - 10^{-5}$ rad and the complete azimuth. The primary angular grid uses 61 polar and 97 azimuthal nodes. This observable contains particle-scattered radiation, including the support-mediated contribution, but excludes the bare-foil reflected plane wave. It is not a supported-sample extinction cross-section or total reflectance.

S8 Spectral and sensitivity results

The baseline sampled maxima are 595 nm for $\bar{K}$, 680 nm for the pump-only proxy and 580 nm for upward scattering. The nominal maximum mean kernel is 2.7860×10^5. Endpoint spectra are shown in Fig. S4. Each tabulated maximum is conditional on the spectral window and equal two-site occupancy.

Table S7. Sampled mean-kernel maxima for the baseline and one-factor spectral endpoints. Maxima use 5 nm local refinement around coarse-grid peaks.

Oxide (nm)	Spacer (nm)	Gap (nm)	Sampled peak pump (nm)	Peak mean kernel
3	5	20	595	278597
1	5	20	595	252355
5	5	20	595	299860
3	3	20	605	178931
3	7	20	595	355621
3	5	10	670	3.26925e+06
3	5	30	585	89677.7

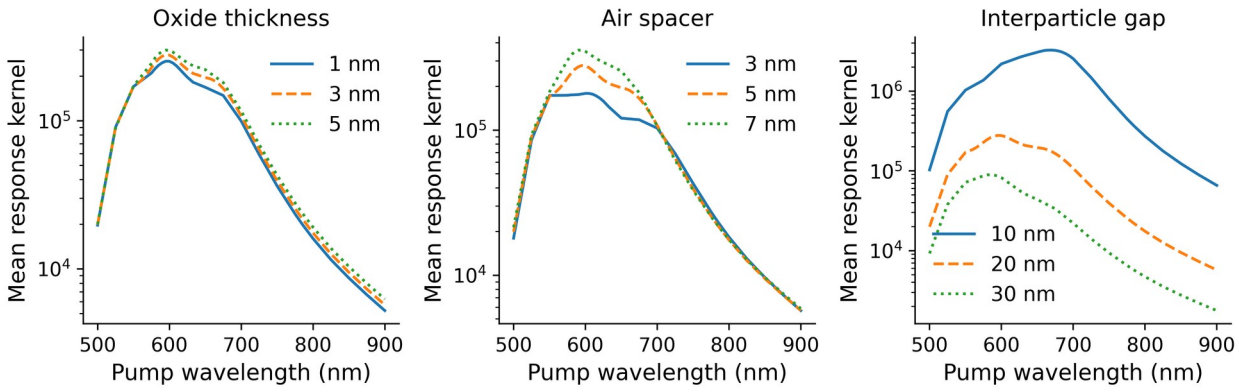


Fig. S4 Mean-kernel spectra for the baseline and the two endpoints of each geometry range. (a) Oxide thickness at fixed s = 5 nm and g = 20 nm. (b) Air spacer at fixed t = 3 nm and g = 20 nm. (c) Interparticle gap at fixed t = 3 nm and s = 5 nm. Sphere radius is 60 nm and reporter weights are ½,½ throughout. Lines connect calculated points; vertical axes are logarithmic

Table S8. Finite-step sensitivities and response spans over the five tested levels. These are deterministic model comparisons, not statistical confidence intervals.

Parameter	Pump (nm)	Normalized finite sensitivity	Maximum/minimum span
Oxide	633	0.191730	1.291760
Oxide	785	0.130686	1.189940
Spacer	633	0.855589	1.951797
Spacer	785	-0.061164	1.065963
Gap	633	-4.909221	54.408419
Gap	785	-5.062732	63.879402

S9 Numerical verification of the extended study

The new calculations evaluate the same top-layer Sommerfeld coupling [S1] using matrix products grouped by azimuthal multipole index. This is a vectorized evaluation of the coupled Maxwell system, not a dipolar or stationary-phase approximation. Upstream Cython direct translations were used, and the same diagonal similarity scaling was retained for the linear solve. Reflected local fields were evaluated in double precision. The vectorized coupling agrees with an upstream sixth-order test block to relative Frobenius error 1.07×10^{-11}; a separate four-frequency eighteenth-order comparison reproduces the existing benchmark projected intensities within the recorded numerical precision.

Primary scans use $\ell_{max} = m_{max} = 20$, an effective-index contour through 0, 0.8, 0.8 − 0.1i, 3.5 − 0.1i, 3.5 and 50, maximum contour step 0.02, and 96 azimuthal intervals for reflected fields. Checks increase the multipole cutoff to 24, contour truncation to 70, reduce the step to 0.01, increase imaginary depth to 0.15 and double the azimuthal sampling to 192. Every geometry is checked at 633 and 785 nm; the seven spectral geometries are additionally checked at their sampled Raman maxima. The target is less than 0.5% change in the reported site intensities and kernels at those tested points. This sampled verification does not provide a rigorous error bound at every untested wavelength.

Table S9. Geometry-grouped maxima of the tested numerical-refinement differences. Raw paired fields and individual check wavelengths are retained in the computational package.

Oxide (nm)	Spacer (nm)	Gap (nm)	Max intensity change (%)	Max site K change (%)	Mean K change (%)
1	5	20	0.00961	0.01703	0.01681
2	5	20	0.00740	0.01194	0.01185
3	3	20	0.01757	0.02642	0.01198
3	4	20	0.00564	0.00903	0.00891
3	5	10	0.06573	0.11752	0.11751
3	5	15	0.00772	0.01418	0.01414
3	5	20	0.01063	0.01806	0.01793
3	5	25	0.00980	0.01529	0.01510
3	5	30	0.01276	0.02359	0.02293
3	6	20	0.01005	0.01541	0.01534
3	7	20	0.01157	0.01850	0.01847
4	5	20	0.00850	0.01380	0.01372
5	5	20	0.01116	0.01864	0.01855

Doubling the far-field angular sampling to 121 polar and 193 azimuthal nodes changes the upward cross-section by at most 0.01586% over the baseline spectral maxima and the two reference pumps. The largest retained linear-system residual in the study is 2.95×10^{-15}.

The package retains all sampled wavelengths, geometries, full complex local fields, outgoing multipole coefficients, integration contours and normalization conventions. CSV outputs reconstruct the plotted curves, central differences and geometry-dependent maxima. No measured substrate morphology, adsorption distribution, chemical enhancement, finite-aperture Raman collection or concentration detection limit is inferred. Simultaneous oxide–spacer–gap interactions require a separate factorial study.

Supplementary references

[S1] Egel A, Czajkowski KM, Theobald D, Ladutenko K, Kuznetsov AS, Pattelli L (2021) SMUTHI: a Python package for the simulation of light scattering by multiple particles near or between planar interfaces. J. Quant. Spectrosc. Radiat. Transf. 273:107846. https://doi.org/10.1016/j.jqsrt.2021.107846

[S2] Johnson PB, Christy RW (1972) Optical constants of the noble metals. Phys. Rev. B 6:4370–4379. https://doi.org/10.1103/PhysRevB.6.4370

[S3] Rakić AD, Djurišić AB, Elazar JM, Majewski ML (1998) Optical properties of metallic films for vertical-cavity optoelectronic devices. Appl. Opt. 37:5271–5283. https://doi.org/10.1364/AO.37.005271

[S4] Polyanskiy MN (2024) Refractiveindex.info database of optical constants. Sci. Data 11:94. https://doi.org/10.1038/s41597-023-02898-2